Sentinel-1 snow depth retrieval at sub-kilometer resolution over the European Alps

Hans Lievens[1], Isis Brangers[1], Hans-Peter Marshall[2], Tobias Jonas[3], Marc Olefs[4], and Gabriëlle De Lannoy[1]

[1]Department of Earth and Environmental Sciences, KU Leuven, Leuven, Belgium
[2]Department of Geosciences, Boise State University, Boise, ID, USA
[3]WSL - Institute for Snow and Avalanche Research SLF, Davos, Switzerland
[4]ZAMG - Zentralanstalt für Meteorologie und Geodynamik, Vienna, Austria

Correspondence: Hans Lievens (Hans.Lievens@KULeuven.be)

Abstract. Seasonal snow in mountain regions is an essential water resource. However, the spatio-temporal variability in mountain snow depth or snow water equivalent (SWE) at regional to global scales is not well understood due to the lack of high-resolution satellite observations and robust retrieval algorithms. We **investigate** the ability of the Sentinel-1 mission to monitor weekly snow depth at sub-kilometer (100 m, 300 m and 1 km) resolutions over the European Alps, for 2017–2019. The Sentinel-1 backscatter observations, especially in cross-polarization, show a high correlation with regional model simulations of snow depth over Austria and Switzerland. The observed changes in radar backscatter with the accumulation or ablation of snow are used in **an empirical** change detection algorithm to retrieve snow depth. The algorithm includes the detection of dry and wet snow conditions. **Compared to in situ measurements at 743 sites in the European Alps, the snow depth retrievals at 1 km resolution have a spatio-temporal correlation between 0.84 and 0.90, depending on the masking of wet snow. The mean absolute error equals 20–30 % for snow depths between 1 and 3 m. The performance slightly degrades for retrievals at increasingly finer resolutions (300 m, 100 m).** The results demonstrate the ability of Sentinel-1 to provide snow estimates in mountainous regions where satellite-based estimates of snow mass are currently lacking. The retrievals can improve our knowledge of seasonal snow mass in areas with complex topography and benefit a number of applications, such as water resources management, flood forecasting and numerical weather prediction. **However, future research is recommended to further investigate the physical basis of the sensitivity of Sentinel-1 backscatter observations to snow accumulation**.

Copyright statement.

1 Introduction

In the European Alps, the release of precipitated water to discharge is delayed by storage in snow and glaciers. During the spring and summer, when water demand is high, snow and glacier meltwater sustains the more than 14 million inhabitants across 8 countries within the Alpine region, e.g., by supplying water for domestic use, industry, hydropower production, agriculture,

etc. However, climate change causes mass loss of most glaciers (Zemp et al., 2019) and perturbs snowmelt dynamics (Bormann et al., 2018; Pulliainen et al., 2020), changing the timing and magnitude of water availability (Immerzeel et al., 2020). An improved monitoring of snow water resources can help strengthening our understanding of these changing hydrological processes in mountain regions.

Remote sensing can play an essential role in the monitoring of snow water resources. The current operational satellite retrievals of snow depth (or snow water equivalent, SWE, using auxiliary snow density information) rely primarily on passive microwave observations, either based only on remote sensing data (Kelly et al., 2003), or in combination with in situ measurements as in GLOBSNOW (Takala et al., 2011). Unfortunately, passive microwave observations have shortcomings, especially in mountain areas. The coarse footprints ($\sim$25 km) cannot resolve the high spatial variability in snow depth imposed by complex topography (Dozier et al., 2016), and the microwave observations have a tendency to saturate at $\sim$0.8 m snow depth, which is often exceeded in mountains (Foster et al., 2005; Tedesco and Narvekar, 2010). Furthermore, missing details about the snow microstructure and layering complicate the physically-based retrievals (Lemmetyinen et al., 2018). Therefore, new and robust satellite observations are critically needed to fill the mountain-snow observation gap (Bormann et al., 2018).

Active microwave observations from Synthetic Aperture Radar (SAR) show promise for mapping snow depth or SWE at a high spatial resolution. The optimal frequencies for global-scale snow observations are likely within X- to Ku-band ($\sim$8–18 GHz) (Rott et al., 2010), based on their strong scattering within the snow volume (Yueh et al., 2009; King et al., 2015). Unfortunately, high-resolution Ku-band satellite observations are not available at present. Alternatively, the use of SAR interferometry (InSAR) (Guneriussen et al., 2001; Leinss et al., 2015; Conde et al., 2019) allows for tracking changes in SWE from changes in the radar signal phase that are caused by refractions in the snowpack. For this approach, lower frequencies such as L-band (1-2 GHz) are preferred, maintaining a better coherence between repeat observations. A number of future missions are addressing the use of L-band InSAR for snow applications, such as the National Aeronautics and Space Administration (NASA) - Indian Space Research Organisation (ISRO) SAR (NISAR) and potentially the Radar Observing System for Europe - L-Band (Rose-L).

Currently, routine SAR backscatter observations with a high spatial resolution ($\sim$20 m) and frequent revisit (<weekly) are only available at C-band (5.4 GHz) from the European Space Agency (ESA) and Copernicus Sentinel-1 (S1) mission. Despite the availability of these routine observations, limited attention has been drawn to the use of C-band backscatter for snow monitoring, after earlier satellite observations had shown a limited sensitivity (Rott and Nagler, 1993; Bernier and Fortin, 1998; Bernier et al., 1999; Shi and Dozier, 2000). However, these studies were mostly focused on relatively shallow snow depths (below $\sim$1 m) and were investigating the use of backscatter observations in co-polarization. At C-band, co-polarized backscatter is generally dominated by (i) the scattering from the ground surface (depending on the moisture content and the temperature or freeze-thaw state of the soil) in dry snow conditions, or by (ii) the absorption by liquid water in wet snow conditions (Baghdadi et al., 1997; Nagler and Roth, 2000; Luojus et al., 2007; Nagler et al., 2016).

Although further research is needed to improve our basic understanding of the physical scattering mechanisms, we hypothesize that cross-polarized observations at C-band are more sensitive to dry snow accumulation than co-polarized observations for two main reasons. First, the surface scattering from the ground is significantly weaker in

cross-polarization due to the limited depolarization that occurs at the ground surface, especially for smooth surfaces. Second, dry snow is expected to enhance scattering in cross-polarization. More specifically, dry snow represents a multi-layered, dense medium of irregularly shaped (anisotropic) ice crystals that can form larger-scale clusters. Signal depolarization can for instance occur due to scattering within the dense anisotropic snow volume, multiple scattering on snow layer interfaces and snow-ground scattering interactions (Du et al., 2010; Chang et al., 2014; Leinss et al., 2016). Hence, in cross-polarized observations, the scattering from the ground surface may no longer dominate over the scattering from the snow (Shi and Dozier, 2000; Pivot, 2012), especially for deep snow that is often encountered in mountain regions.

Recently, Lievens et al. (2019) demonstrated the sensitivity of S1 cross-polarized backscatter observations to dry snow accumulation and developed an **empirical** change detection algorithm to retrieve snow depth at 1 km spatial resolution over all mountain ranges in the Northern Hemisphere. The retrievals are based on a number of assumptions that, in the case of C-band, are likely more valid for deeper snow. **That is, (i) an increase in snow depth causes an increase in snow scattering especially in cross-polarization, (ii) the snow scattering contribution is not negligible compared to the ground scattering contribution, and (iii) the ground scattering contribution remains relatively constant during the winter period because of the limited changes in soil temperature (due to the insulating properties of snow), soil moisture and surface roughness, such that (iv) the main changes in backscatter over time can be related to changes in the snowpack.**

Here, we further refine the S1 snow depth retrievals and evaluate them at 100 m, 300 m and 1 km over the European Alps for the two year period from August 2017 through July 2019. First, The sensitivity of the S1 backscatter observations in co- and cross-polarization is evaluated using regional model simulations of snow depth over Austria and Switzerland and stratified by elevation and forest cover fraction. Thereafter, S1 snow depth retrievals at three resolutions are regionally optimized using auxiliary information on topography and land cover. Finally, the accuracy of the retrievals is estimated based on independent time series measurements at 743 in situ locations across the Alps.

The results of this study contribute to improving our knowledge of seasonal snow mass in areas with complex topography and thereby addresses a long-standing observation gap in the remote sensing of the cryosphere. A strong asset is the assured long-term continuity of S1 C-band SAR observations over the coming decades, which will allow for analyzing trends in snow mass impacted by climate variability or climate change. Finally, the S1 snow depth retrievals could be of high value for data assimilation into land surface models (Girotto et al., 2020). Not only could the assimilation ensure improved and continuous (in time and space) estimates of various snow variables, it is likely to also benefit applications such as flood forecasting (Dechant and Moradkhani, 2011; Griessinger et al., 2019) or numerical weather prediction (de Rosnay et al., 2014). **Future research is recommended to further investigate the physical scattering mechanisms in snow at C-band, including the impacts of snow microstructure and stratigraphy, and to extend the validation over regions with different soil, vegetation and snow conditions, also using validation data at the matching scale of the satellite retrievals**.

2 Data and methods

2.1 Sentinel-1 observations

The S1 mission is a constellation of two satellites, S1A and S1B, launched in April 2014 and 2016, respectively. Over land and outside the polar regions, S1 routinely operates in the Interferometric Wide Swath (IW) mode, acquiring backscatter observations at ∼20 m resolution in vertical-vertical (VV) and vertical-horizontal (VH) polarizations. We processed the IW S1A and S1B ground-range detected (GRD) data for the period August 1, 2017 to July 31, 2019 over the European Alps (∼4600 images). The processing was performed using the ESA Sentinel Application Platform (SNAP) toolbox, applying standard processing techniques: **precise orbit file application, GRD border noise removal, thermal noise removal, radiometric calibration, terrain flattening to backscatter as γ^0 (Small, 2011; Small et al., 2021), range-Doppler terrain correction, and aggregation to 100 m by linear averaging with projection onto the World Geodetic System WGS84 geopgraphic coordinate system. The terrain flattening and terrain correction were applied using digital elevation data from the Shuttle Radar Topography Mission (SRTM) at 1 arcsecond resolution, which is similar to the original resolution of S1. The 100 m grid cell size in the processed output was chosen to reduce the speckle noise inherent to radar observations, to reduce the impacts of geometric distortions (e.g., radar foreshortening, layover, shadowing, and inaccuracies in the geo-referencing) within the complex topography of the Alps, and to improve the feasibility of the processing by reducing the processing time and storage requirements.**

The S1A and S1B satellites have an exact 12-day repeat cycle, with 175 orbits per cycle. As both satellites share the same orbital plane with a 6-day offset, the two-satellite constellation offers an exact 6-day repeat cycle. Depending on the region, more frequent observations (2–3 days on average) are available due to orbits with partly overlapping swaths and the combination of ascending and descending tracks. **Over repeating cycles, acquisitions from a given orbit consistently observe the same grid cell with the same incidence and azimuth angle, and should thus provide unbiased repeated samples. However, the γ^0 observations from different orbits can still show remaining biases due to the different viewing geometries. To reduce this bias,** we pooled **all** γ^0 values pertaining to the same orbits into separate time series. For each orbit, we calculated the first and second order moment statistics (temporal mean and standard deviation), and scaled the γ^0 values (in dB) such that these statistics match the average statistics across all orbits:

$$\gamma^0_{\mathrm{bc},o} = <\overline{\gamma^0_o}> + \left(\gamma^0_o - \overline{\gamma^0_o}\right) \frac{<\mathrm{std}\left(\gamma^0_o\right)>}{\mathrm{std}\left(\gamma^0_o\right)} \tag{1}$$

with $\gamma^0_{\mathrm{bc},o}$ the bias-corrected backscatter for orbit o, $\overline{\gamma^0_o}$ the temporal mean backscatter for orbit o, $\mathrm{std}\left(\gamma^0_o\right)$ the temporal standard deviation in backscatter for orbit o, and $<>$ denoting the average over the different orbits. This procedure ensures unbiased γ^0 values in the mean and standard deviation across orbits. Note that for the calculation of the time series statistics (mean and standard deviation), we excluded observations from March through July, to avoid strong γ^0 fluctuations caused by wet snow, with potentially large differences between 6 am descending and 6 pm ascending tracks in case of refreezing.

Deleted: "For a given 100 m grid cell, the S1 observations from different orbits within one repeat cycle have a different viewing geometry, in terms of look direction, incidence angle and azimuth angle. Particularly in mountainous areas, the impact of these different viewing geometries on σ^0 can be large, for instance when a terrain slope is facing towards or away from the sensor line of sight, and thus needs to be accounted for. To reduce these effects, we corrected σ^0 for the local incidence angle (θ; in degrees), i.e., the angle between the radar line of sight and the normal to the local surface. The local surface was derived from the Shuttle Radar Topography Mission (SRTM) digital elevation model (projected onto the 100 m WGS84 grid). The σ° correction to the 40° reference incidence angle was based on the frequently applied cosine approximation (Ulaby et al., 1982; Bernier and Fortin, 1998):

$$\sigma^0_{40^\circ} = \sigma^0 \frac{\cos 40^\circ}{\cos \theta} \tag{2}$$

Future research is recommended to investigate the use of observations processed to terrain-flattened backscatter (γ^0), which offers an improved correction for the local incidence angle by also taking into account its impact on the illuminated area (Small, 2011; Small et al., 2021).

As the final processing step, we performed an outlier correction, by replacing values that differ more than ± 1.5 dB from the mean σ^0 calculated over a 12-day window by the mean value. The 12-day window was selected as this corresponds with the S1 repeat cycle and thus ensures the inclusion of observations obtained from the same platform (S1A or S1B) and orbit."

Finally, we averaged the γ^0 observations to weekly values. The result of the processing is thus weekly 100 m γ^0 backscatter (dB) in co- and cross-polarization over the Alps, obtained after applying standard processing, an orbit-bias correction and the merging of ascending and descending S1A and S1B observations. In the remainder of the text, we denote the final processed backscatter values as γ^0 for simplicity.

2.2 Snow depth retrievals

The snow depth retrieval algorithm is based on the **assumption** that **a snowpack is typically composed of multiple snow layers, where each of the layers represents a dense medium of clustered, irregularly-shaped (anisotropic) ice crystals within an air background. We hypothesize that the microwave signal in the snowpack depolarizes primarily by the scattering on anisotropic clusters of snow crystals within the snow volume (Chang et al., 2014), by the multiple scattering between snow layer interfaces (Du et al., 2010), and by snow-ground scattering interactions. A deeper snowpack is likely to result in more opportunities for signal depolarization and therefore stronger scattering in cross-polarization. Hence, the strength of the cross-polarized scattering can be related with snow depth. While higher microwave frequencies (such as X- and Ku-band) are likely more suitable to detect snow scattering in shallow snow environments, we hypothesize that the contribution at C-band is large enough for application to the typically deep snow regimes in mountain areas. The algorithm further assumes that snow scattering generally has a stronger contribution in cross-polarized (VH in the case of S1) compared to co-polarized (VV) observations, whereas scattering impacts from soil moisture, soil freeze/thaw or soil temperature are expected to be more similar in co- and cross-polarization. Therefore, the use of a ratio (in linear scale, or difference in dB scale) between cross- and co-polarization γ^0 observations can reduce the impacts of ground,**

vegetation and surface geometry properties, and enhance the sensitivity to snow depth (Bernier et al., 1999; Lievens et al., 2019).

The empirical retrieval method based on change detection builds further on Lievens et al. (2019) and the main differences with this study are highlighted in this section. As auxiliary input, the algorithm requires snow cover (SC) absence/presence observations, which we derived from the 1 km resolution Interactive Multisensor Snow and Ice Mapping System (IMS; National Ice Center (2008)) dataset, **glacier cover fraction (GCF), derived from the Randolph Glacier Inventory 6.0 (RGI Consortium, 2017)**, and forest cover fraction (FCF), derived from the 100 m Copernicus PROBA-V dataset (Buchhorn et al., 2020).

Firstly, the change detection algorithm from Lievens et al. (2019) has been modified to account for the observation that, for sparsely vegetated areas, a ratio of VH- and VV-polarized γ^0 (cross-polarization ratio; CR) shows the highest correlation with snow depth, whereas in more densely forested areas, the VV-polarized γ^0 shows a higher temporal correlation (see Fig. 5 below). The latter may be caused by the relatively stronger scattering contribution from forests (and vegetation in general) in VH-polarization (Vreugdenhil et al., 2020), decreasing the sensitivity to the underlying snowpack. Therefore, two change detection indices (SI1 and SI2; in dB) are calculated for each location i and weekly time step t:

$$\mathrm{SI1}(i,t) = \mathrm{SI1}(i,t-1) + \left[\gamma^0_{\mathrm{CR}}(i,t) - \gamma^\circ_{\mathrm{CR}}(i,t-1)\right] \tag{3}$$

$$\mathrm{SI2}(i,t) = \mathrm{SI2}(i,t-1) + \left[\gamma^0_{\mathrm{VV}}(i,t) - \gamma^\circ_{\mathrm{VV}}(i,t-1)\right] \tag{4}$$

where γ^0_{CR} represents a weighted combination of cross-polarized γ^0_{VH} and co-polarized γ^0_{VV} observations (in dB) of the general form:

$$\gamma^0_{\mathrm{CR}} = A\gamma^0_{\mathrm{VH}} - \gamma^0_{\mathrm{VV}} \tag{5}$$

with A being a fitting parameter. SI1 and SI2 are set to zero when snow cover (SC) is absent, or in case of negative values. Strong temporal changes in SI (above 1 dB) are reduced (by a factor of 0.25) to avoid outliers. Further, SI1 and SI2 are scaled and combined based on the PROBA-V forest cover fraction (FCF (-); ranging from 0 to 1):

$$\mathrm{SI} = (1-\mathrm{FCF}) \cdot \frac{1}{1 - B \cdot \mathrm{FCF}} \cdot \mathrm{SI1} + \mathrm{FCF} \cdot C \cdot \mathrm{SI2} \tag{6}$$

with B and C fitting parameters. **Similarly, SI is scaled over glaciated areas to account for the relatively stronger increase in γ^0 during winter (see Fig. 3 below), which is likely a combined effect of snow accumulation and the freezing of glacial meltwater. The scaling based on glacier cover fraction (GCF (-); ranging from 0 to 1) is given by:**

$$\mathrm{SI_{gl}} = [D + (1-D) \cdot (1-\mathrm{GCF})] \cdot \mathrm{SI} \tag{7}$$

The four algorithm parameters were iterated over $A \in [1:1:3]$, $B \in [0:0.1:1]$, $C \in [0:0.1:2]$ and $D \in [0:0.1:1]$, and optimized based on model simulations of snow depth (optimization not shown; simulations described in Section 3.1). This resulted in $A = 2$, $B = 0.2$, $C = 0.8$ and $D = 0.5$, which are further used in this study. Deleted: "Note that the

optimized value for B is similar to the value of 0.6 used in Lievens et al. (2019), which is also used in the operational passive microwave retrievals (Tedesco and Narvekar, 2010)."

Secondly, $\mathrm{SI_{gl}}$ (in dB) is translated into snow depth (or height of snow, HS, in m) by multiplication with an empirical scaling parameter E:

$$\mathrm{HS}(i,t) = E \cdot \mathrm{SI_{gl}}(i,t) \tag{8}$$

The value of E is estimated by minimizing the absolute bias between the retrieved and the modeled snow depth (Section 3.1). Note that the scaling based on model simulations can propagate simulation uncertainties into the retrieval. Two estimates for E are proposed, i.e. E_1 and E_2. As a first approximation, E_1 is considered constant in space and time, conform with Lievens et al. (2019). **This approach is applicable to mountain ranges for which no detailed information on the spatial snow depth distribution, e.g., provided by model simulations, LiDAR data or dense networks of in situ measurements, is available.** The E_1 value that minimizes the bias against the model simulations here equals 0.45 m/dB. Thus, a 1 dB temporal change in the input γ^0 ratio on average corresponds with a 0.45 m change in snow depth. Besides a constant scaling factor, we also investigate a more optimized estimation of E_2 that varies in space **(but not in time)**, depending on auxiliary information of topography (SRTM elevation) and land cover (Copernicus PROBA-V classification). Therefore, E_2 is obtained by first stratifying the optimization by elevation (i.e., selecting the value that minimizes the bias per elevation band, ranging from 50 m to 3500 m in steps of 100 m), and subsequently stratifying the optimization by land cover class. **Note that such approach may improve the spatial distribution of the snow depth retrievals, but is only feasible in regions where sufficient reference information is available.**

Thirdly, as an extension to Lievens et al. (2019), we here include a wet snow detection algorithm to **flag** the S1 retrievals in wet snow conditions. Wet snow is known to absorb a large part of the radar signal, causing a strong decrease in γ^0 (e.g., Baghdadi et al., 1997; Nagler and Roth, 2000; Luojus et al., 2007; Nagler et al., 2016; Marin et al., 2020) that can result in an underestimation in snow depth. **Three different wet snow detection mechanisms are implemented. The first mechanism aims to detect wet snow early in the snow season, i.e., from the start of the season until the end of December. The second and third mechanisms are applied from January onward, and the resulting wet snow flags are retained from the first detection until the snowpack is completely melted, to avoid that uncertainties induced by wet snow propagate into subsequent retrievals.**

The first mechanism accounts for the observation that early snowfall often leads to γ^0 values that are lower than in snow-free conditions, likely because the snowfall is wet or the snow accumulation is moistening/melting soon after the snowfall event. Therefore, wet snow is classified if γ^0 (either in VV- or VH-polarization) decreases more than a threshold (2 dB) below the lower 10-th percentile of the snow-free γ^0 observations between August and the end of December.

The second mechanism aims at detecting wet snow later in the season, after liquid water in the snowpack absorbs the signal. Therefore, the wet snow detection criterion applied for each weekly time step t is based on the decrease rate of γ^0:

$$\gamma^0_{\mathrm{VH}}(t+1) - \gamma^0_{\mathrm{VH}}(t-1) < F \quad \text{or} \quad \gamma^0_{\mathrm{VV}}(t+1) - \gamma^0_{\mathrm{VV}}(t-1) < F \tag{9}$$

with F a threshold set to **-1.5 dB**. Note that we here refrain from detecting wet snow based on the difference in γ^0 with a (constant) dry snow reference value, as often done in the literature (e.g., Baghdadi et al., 1997; Nagler et al., 2016; Tsai et al., 2019; Manickam and Barros, 2020), because of the difficulty to accurately define the dry snow reference value (Manickam and Barros, 2020). For instance, an average summer γ^0 is often used as an approximation of the dry snow reference (Tsai et al., 2019; Manickam and Barros, 2020). However, in regions with dense vegetation, summer γ^0 can be high due to vegetation contributions, causing an over-detection of wet snow in winter if γ^0 is systematically lower. Conversely, in bare or sparsely vegetated regions, snow accumulation can cause a significantly higher γ^0 (by several dB) compared to the summer reference, requiring a large decrease from wet snow to reach the threshold below the summer reference (see below, e.g., Fig. 4). The use of a fixed dry snow reference value is here avoided by thresholding the decrease rate of γ^0 over time instead.

The third mechanism mainly addresses regions where no strong decrease in γ^0 is observed due to a lower sensitivity to snow wetness. This is for instance expected in more shallow or patchy snow cover, or in forested regions where the snow signal is attenuated and the vegetation contributes to the scattering. In this case, the snow state is classified as wet if SI becomes lower than zero.

Using the **empirical framework** outlined above, we processed snow depth retrievals for the 2 year period from August 1, 2017 to July 31, 2019 over the entire European Alps. **The retrievals are performed at 100 m spatial resolution, but outputs are produced at three different spatial resolutions, i.e., 100 m, 300 m and 1 km, to assess the impact of the spatial resolution on the retrieval performance.** The 300 m and 1 km snow depth retrievals are obtained by linearly averaging the 100 m retrievals. **The binary information on the dry/wet snow state at 100 m resolution is also linearly averaged to the coarser scales, resulting in fractional wet snow cover information that ranges between 0 and 1.** Finally, note that the retrievals at the finer scales (i.e., 100 m, 300 m) use the same relationship of E_2 with elevation and land cover, as established based on the 1 km data, because the snow depth model simulations used for the optimization are only available at the 1 km scale.

2.3 Model simulations

Output from two regional snow models for Austria (SNOWGRID-CL) and Switzerland (OSHD) is used to assess the S1 backscatter and to optimize the snow depth retrievals. Fig. 1 shows that the joint simulation domain covers a large part of the Alps. For the comparison with the weekly 1 km S1 observations, the model simulations of snow depth from the SNOWGRID-CL and OSHD are averaged from the daily to the weekly time scale. In addition, simulations by the Noah-Multiparameterization (Noah-MP) land surface model (Niu et al., 2011) are used to assess the impacts of soil moisture and soil temperature on S1 backscatter.

SNOWGRID-CL (Olefs et al., 2020) is the climate version of the spatially distributed snow model ran operationally at ZAMG with a daily timestep on a 1 km grid over Austria. The model outputs snow depth and SWE, and is forced with daily 1 km gridded meteorological data of air temperature, precipitation and evaporation that take into account the high variability of these variables in complex terrain (Hiebl and Frei, 2016, 2018; Haslinger and Bartsch, 2016). The model solves the shortwave radiation balance following Pellicciotti et al. (2005) and uses a simple 2-layer snow scheme, considering settling, the exchange

of heat and liquid water content, and energy addition by rain. Lateral snow mass redistribution is included as a function of snow and terrain properties (Frey and Holzmann, 2015). The accuracy of the daily snow depth simulations (correlation of 0.83, root-mean-square error (RMSE) of 14.11 cm, and bias of -3.12 cm) has been assessed for the period from November through April 2011–2018 (Olefs et al., 2020).

The OSHD (operational snow-hydrological service) multi-model framework provides daily SWE and snowmelt estimates for Switzerland at 1 km spatial resolution. It consists of a suite of spatially distributed snow models integrated with three-dimensional sequential assimilation of snow monitoring data from several hundred sites (Magnusson et al., 2014; Winstral et al., 2019). The models include procedures to account for unresolved variability at the sub-grid scale, two of which are: (1) fractional snow-covered area is parameterized using terrain parameters derived at 25 m spatial resolution according to Helbig et al. (2015); (2) snow distribution and redistribution at small scales is considered using slope- and aspect-dependent transfer functions that were derived from a set of high-resolution snow depth maps from airborne lidar (Grünewald and Lehning, 2015). For this study we use output from the JULES Investigation Model (JIM; Essery et al. (2013)), which is one of the OSHD members. JIM is forced using a combination of numerical weather prediction output from COSMO-1 (www.cosmo-model.org) and reanalysis data as detailed in Winstral et al. (2019), and includes data assimilation from 344 Swiss snow monitoring stations. The assimilation improves the accuracy of the daily snow depth simulations from an RMSE of 21.3-42.4 cm and bias of 4.08-26.1 cm (varies between the years 2014, 2015 and 2017) to an RMSE of 17.3-25.6 cm and bias of 0.8-2.5 cm.

Additional simulations with the Noah-MP land surface model are performed to provide information on soil conditions (SNOWGRID-CL and OSHD are strictly snowpack models). These simulations cover the entire Alps at the daily timescale and are forced using the globally-available Modern-Era Retrospective analysis for Research and Applications, Version 2 dataset (Gelaro et al., 2017). The analyzed model outputs include soil moisture (in m^3 m^{-3}) for the top soil layer (0–0.1 m) and soil temperature (in K) for four soil layers (0–0.1 m, 0.1–04 m, 0.4–1 m and 1–2 m).

2.4 In situ measurements

Weekly average in situ measurements of snow depth for the period August 1, 2017 to July 31, 2019 are assembled for 743 sites, managed by Météo France, WSL–SLF and ZAMG. The locations of the sites are shown in Fig. 2 on top of SRTM elevation and PROBA-V land cover. The minimum, mean and maximum elevations of the measurement sites are 230 m, 1395 m and 3114 m, respectively. **The in situ time series are used to evaluate the temporal and spatial variability of the S1 retrievals in terms of Pearson correlation (R), as well as the bias and mean absolute error (MAE)**.

An inevitable problem in the comparison between S1 observations and in situ measurements is that, particularly in mountain areas, the point-scale snow conditions at the in situ sites not always resemble the grid-scale conditions represented by the satellite data. The local variability in conditions can be large due to differences in elevation, slope and aspect, as well as wind and vegetation impacts on snow distribution (Blöschl, 1999; Seidel et al., 2016; Schattan et al., 2017). Moreover, in situ sites are preferentially located in relatively flat and non-forested terrain, often not representative of the surrounding area displaying

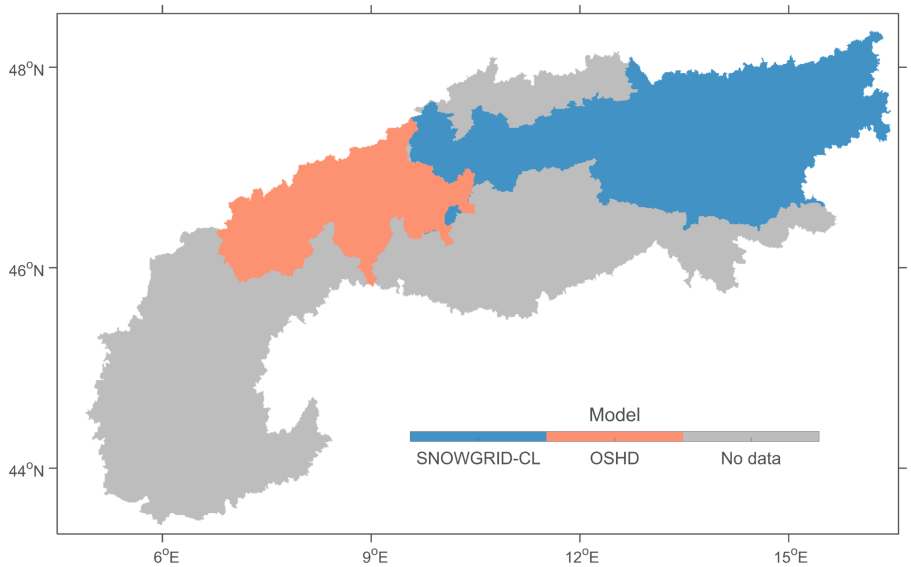

Figure 1. The domains of the 1 km resolution SNOWGRID-CL and OSHD model simulations of snow depth.

large variations in slope and forest cover (Meromy et al., 2013; Grünewald and Lehning, 2015; Dozier et al., 2016), and are underrepresented at high elevations (see Fig. 2).

3 Results and discussion

3.1 Comparison of 1 km S1 observations with snow model simulations

3.1.1 Dynamic range in backscatter

The **dynamic range** in S1 γ^0 in VV- and VH-polarization **and cross-polarization ratio (CR)** with dry snow accumulation is shown in Fig. 3. More specifically, the figure shows the simulated difference between the maximum (weekly) snow depth and the snow depth during the first week with snow cover during the period August–March, as well as the corresponding observed S1 differences in γ^0 between the weeks with the maximum snow depth and first snow cover. **The 1 km γ^0 is obtained by linearly averaging the values at the 100 m scale. Time steps with wet snow are excluded based on the S1 wet snow detection algorithm, when fractional wet snow cover exceeds 0.5. The forest cover fraction from PROBA-V and glacier cover fraction from RGI are also shown to support the analysis.**

In regions with shallow maximum snow depths (<1 m), γ^0_{VV} generally remains relatively constant, with changes typically within $\pm$1 dB (Fig. 3b). Most of the regions with significant snow accumulation, outside glaciated areas, show a slight increase in γ^0_{VV} (about 1–3 dB). The underlying physical mechanisms that cause this increase are still uncertain, but we hypothesize that, in addition to snow volume scattering, the frequent occurrence of snow melt/refreeze cycles may lead to a more complex snow-

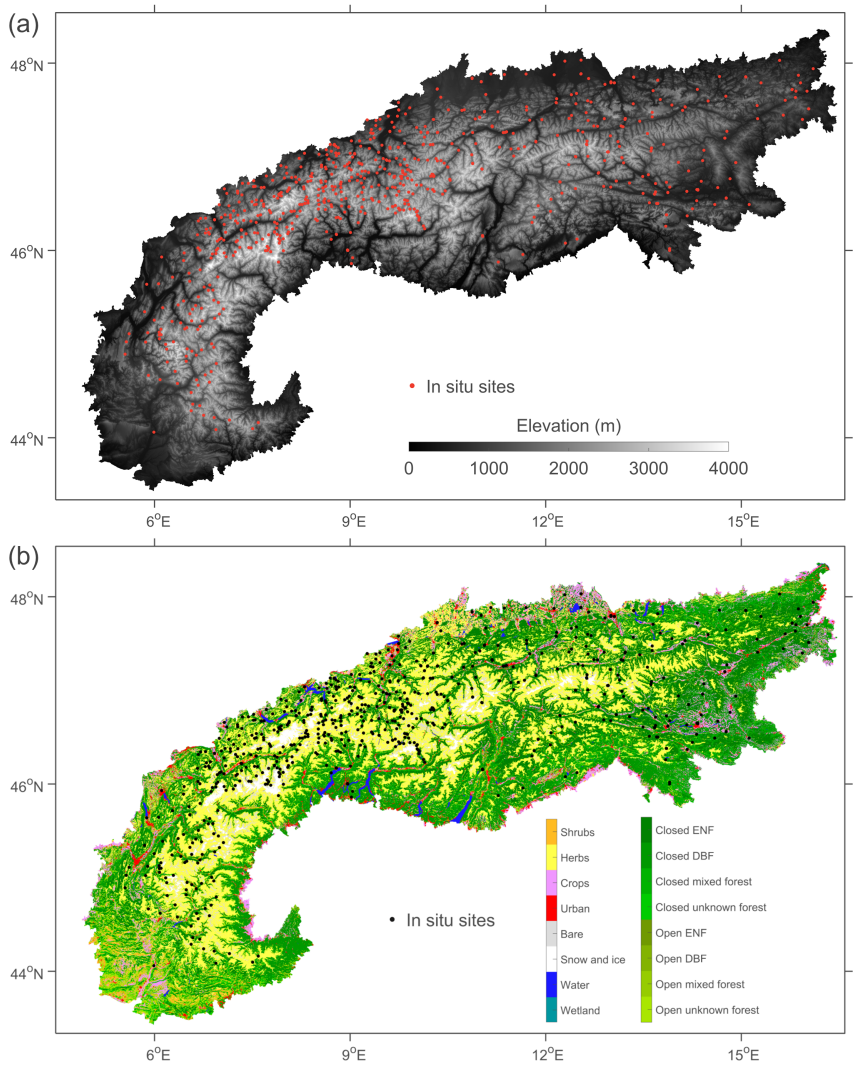

Figure 2. The in situ measurement locations within the European Alps on top of (a) elevation (m) and (b) land cover class (-). **ENF stands for evergreen needleleaf forest, DBF for deciduous broadleaf forest.**

pack with pronounced layering (incl. ice crusts and frozen percolation features) that increases scattering in co-polarization. The increase is mainly observed in areas with a lower γ^0_{VV} during snow-free conditions (not shown). In other regions, particularly at high elevations (above ∼2400 m, but not in glaciated areas), a slight decrease in γ^0_{VV} is observed. At these elevations, melt/refreeze cycles are much less frequent, causing a more homogeneous snowpack from which the scattering contributions in co-polarization are lower compared to the contributions from the ground surface. The slight decrease in γ^0_{VV} in these regions **is likely caused by** the attenuation of the ground surface scattering by the snowpack. Finally, in glaciated areas, a moderate to

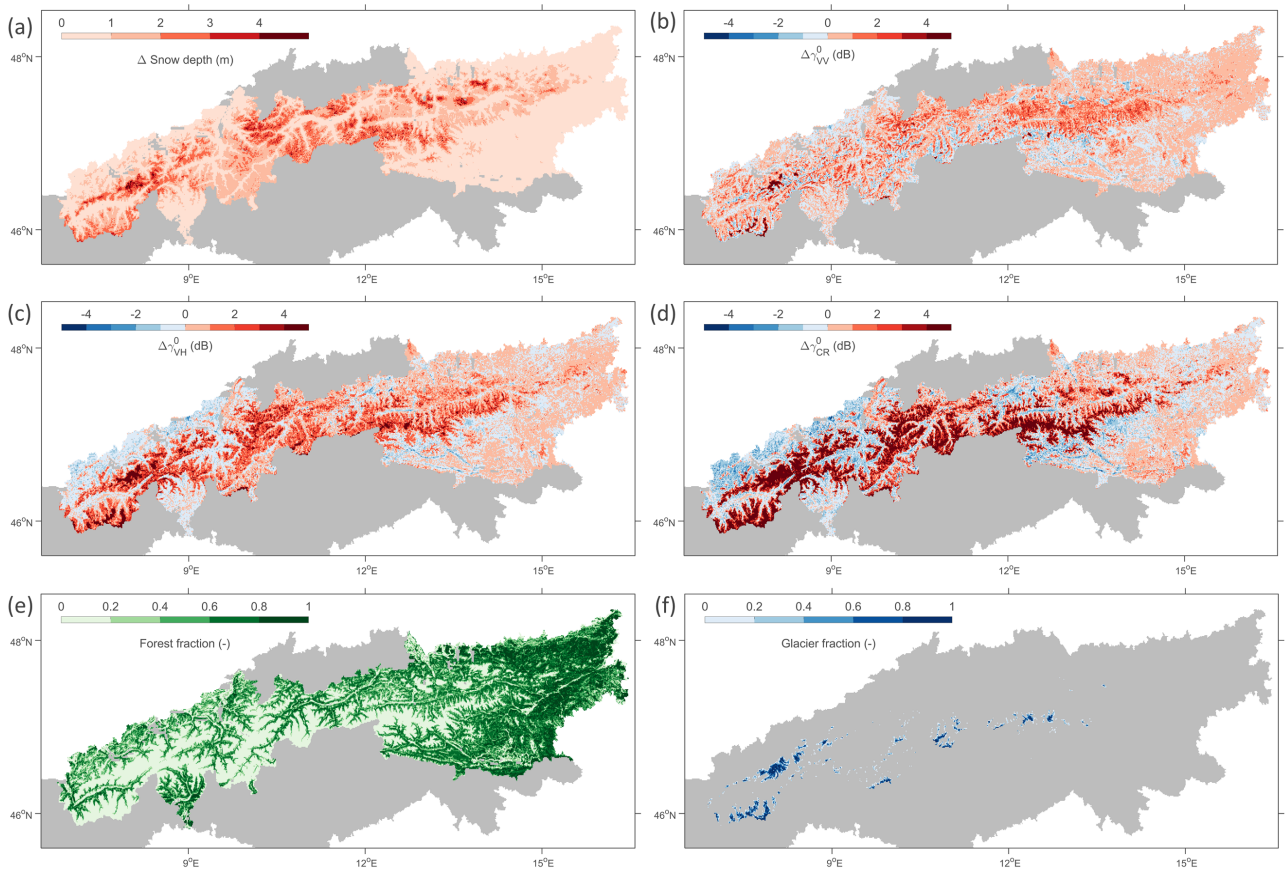

Figure 3. (a) The difference between the maximum weekly 1 km simulated snow depth (m) and the snow depth in the first week with snow cover for August–March (excluding wet snow conditions detected by S1). (b) The corresponding observed difference in S1 γ^0_{VV} (dB). (c) The corresponding difference in S1 γ^0_{VH} (dB). (d) The corresponding difference in S1 γ^0_{CR} (dB). (e) The PROBA-V forest cover fraction (-). (f) The RGI glacier cover fraction (-).

strong increase (4–5 dB or more) is observed, which is likely due to the gradual freezing of glacial meltwater during winter, reducing the absorption of the radar signal through winter.

These results are in close agreement with several previous studies. Rott and Nagler (1993) found a slight decrease in European Remote Sensing (ERS) VV-polarized backscatter observations over a shallow snowpack, but a strong increase over glaciated areas. Bernier and Fortin (1998) and Arslan et al. (2006) observed mostly an increase in co-polarized backscatter during dry snow accumulation, based on RADARSAT and airborne observations, respectively. Shi and Dozier (2000) and Pivot (2012) observed an increase in RADARSAT and ERS co-polarized backscatter (up to several dB) with dry snow accumulation in regions where snow volume scattering was dominating over ground surface scattering, and a slight decrease in regions where the dominant effect was the attenuation of the ground surface scattering by the snowpack.

The signature in γ^0_{VH} (Fig. 3c) shows a more pronounced spatial pattern compared to γ^0_{VV}, with a consistent and moderate to strong increase in γ^0_{VH} (about 3–4 dB) in regions where snow depth reaches above 1 m. We hypothesize that for cross-polarized observations the **scattering from the snowpack** is more consistently dominating over the (attenuated) ground surface scattering. The ground scattering contribution is relatively lower, since it is mostly in the form of surface scattering with limited depolarization (especially for smooth and sparsely vegetated surfaces). The dry snow scattering contribution is stronger, **most likely** because **depolarization occurs after volume scattering on anisotropic crystals or clusters of crystals, multiple scattering on snow layer interfaces, and snow-ground scattering interactions**. As in the γ^0_{VV} observations, the largest increases in γ^0_{VH} (>5 dB) are again observed over glaciated areas, and are likely caused by the combination of freezing glacial meltwater and snow accumulation.

Only a few previous studies have investigated satellite or airborne cross-polarized backscatter observations at C-band in relation with snow depth or snow mass. Some of the heritage satellite missions, such as ERS, did not have the capability to measure in cross-polarization. Moreover, since the 90's, there has been a focus shift towards the use of higher-frequency microwave observations (e.g., in X- and Ku-band), in part due to the limited potential of C-band found with co-polarization, but also in preparation for higher-frequency satellite mission candidates (e.g., CoReH2O). Nevertheless, our results are in agreement with Arslan et al. (2006), who observed a stronger increase in cross-polarization than in co-polarization at C-band with dry snow accumulation. More recently, Lievens et al. (2019) demonstrated the sensitivity of S1 cross-polarized backscatter observations to snow depth over all Northern Hemisphere mountain ranges.

An exception to the overall **stronger snow signal in** S1 γ^0_{VH} is observed in regions with both substantial snow accumulation and dense forest cover. Here, slightly **larger differences** are found for γ^0_{VV}. We hypothesize this may be caused by the relatively stronger scattering from vegetation in cross-polarization (compared to co-polarization), reducing the sensitivity to the scattering contributions from the snowpack. At the same time, forested regions in the Alps are mostly present at lower elevations in the valleys (below ∼2500 m), where an increased occurrence of melt/freeze cycles could result in a more complex and layered snow structure that impacts the polarimetry. **The γ^0_{CR} (Fig. 3d) generally enhances the impact of snow, showing larger increases in backscatter for regions with deep snow compared to γ^0_{VH}. The spatial distribution is however similar to that of γ^0_{VH}, also showing slight decreases in γ^0_{CR} in regions with shallow snow and forest cover, particularly in the western part of the model domain.**

3.1.2 Temporal evolution in backscatter

Figure 4 shows time series examples of γ^0 in VH- and VV-polarization, along with model simulations of snow depth from SNOWGRID-CL and OSHD, and soil moisture and soil temperature from Noah-MP, for two locations in Austria and Switzerland, respectively. The figure corroborates the results shown in Fig. 3. The γ^0_{VH} observations show a strong correspondence with the dry snow accumulation at both locations and for both winter seasons. The evolution in γ^0_{VH} is unlikely to be related to changes in soil moisture or soil temperature. Soil moisture shows a decrease throughout the snow accumulation period, and this would result, if it would have anywere of impact, in a decrease in γ^0. Soil temperature remains nearly constant throughout the snow accumulation period due to the insulating properties of snow. Near the peak of the snow season (although earlier in 2019

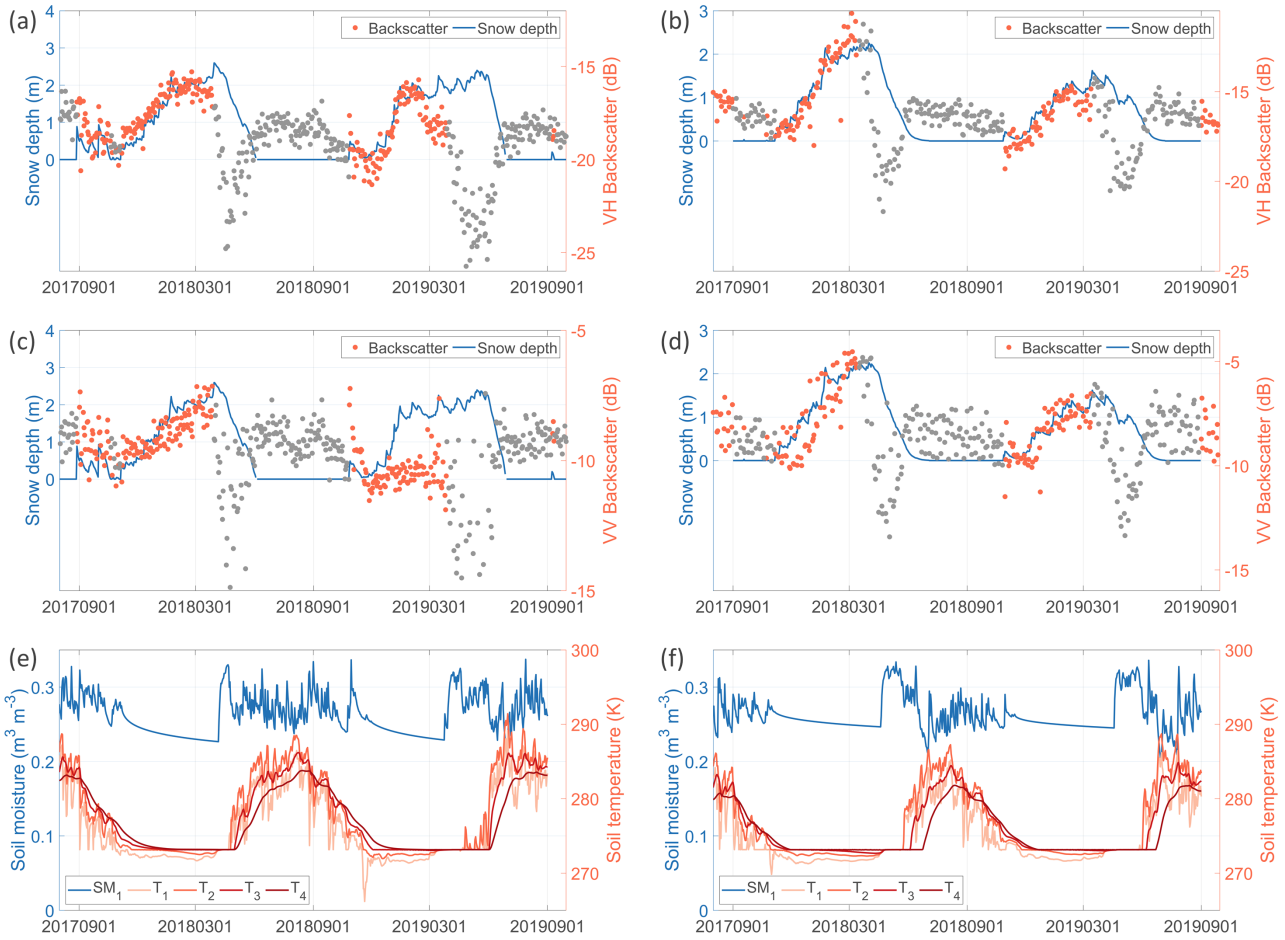

Figure 4. Time series of S1 γ^0 (dB) in (a,b) VH-polarization and (c,d) VV-polarization, compared against model simulations of snow depth (m) for a grid cell in (a,c) Austria (47.1379°N, 11.5923°E, 2355 m, simulations by SNOWGRID-CL) and (b,d) Switzerland (46.0962°N, 7.2569°E, 2140 m, simulations by OSHD). The γ^0 observations during snow-free conditions (derived from the model simulations) and wet snow conditions (derived from the γ^0 data) are displayed in grey. **The γ^0 axes are scaled to enhance visualization.** (e,f) show corresponding model simulations of soil moisture (SM1: 0–0.1 m; in m^3 m^{-3}) and soil temperature (T1: 0–0.1 m, T2: 0.1–04 m, T3: 0.4–1 m and T4: 1–2 m; in K) from the Noah-MP land surface model.

for the location in Austria), the strong decrease in γ^0 is caused by the increase in liquid water content within the snowpack that absorbs the radar signal. The wet snow detection algorithm effectively tracks the onset of the wet snow conditions, and allows for masking the subsequent observations (shown in grey). Note that the first wetting of the snow typically starts before the actual melting phase with shrinking of the snowpack (Marin et al., 2020). The γ^0_{VV} observations correspond well with the snow depth simulations for the location in Switzerland, but less for the location in Austria, in particular during the winter of

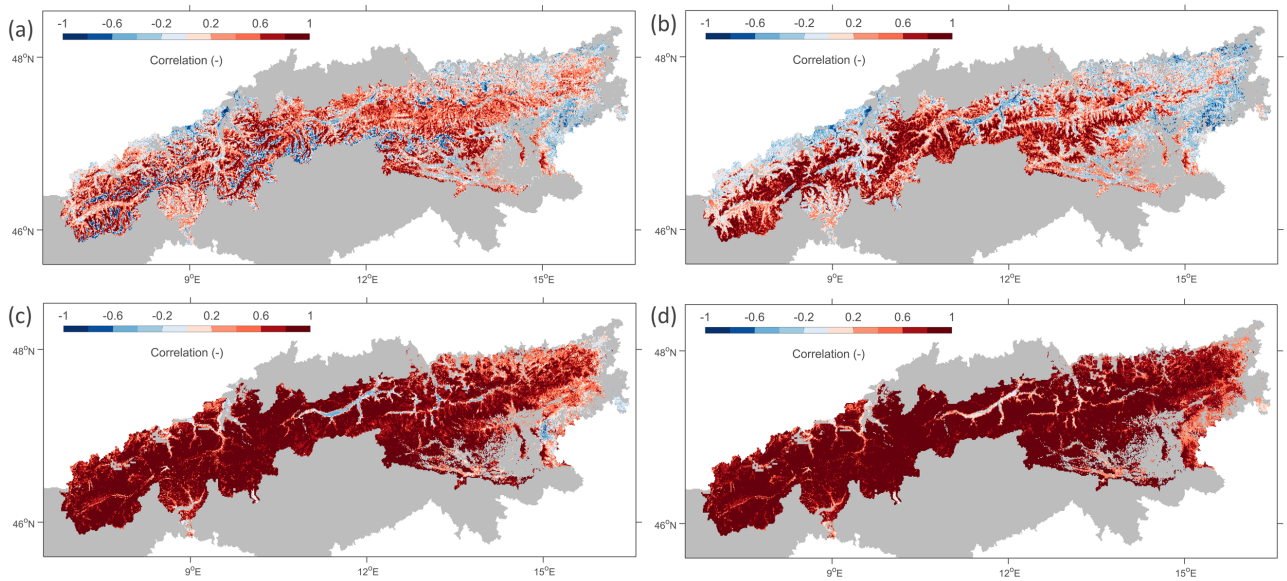

Figure 5. (a) The time series correlation between weekly simulated snow depth (m) and (a) S1 γ^0_{VV} (dB), (b) γ^0_{VH} (dB), (c) S1 snow depth (m), limited to the period with snow cover (based on the model simulations) and dry snow conditions (detected by S1; data with a wet snow fraction larger than 0.5 are excluded), and (d) S1 snow depth (m), limited to the period with dry snow conditions but including zero snow depths.

2018–2019. **There, the γ^0_{VV} is impacted more strongly by the soil moisture content, especially around the start of the snow season, and suggests a more dominant scattering contribution from the ground surface.**

Figure 5 illustrates the time series correlations between the snow depth model simulations and the S1 γ^0_{VV}, S1 γ^0_{VH} as well as the associated S1 snow depth retrievals, for the model domain at 1 km resolution covering Austria and Switzerland. The analysis for Figs. 5a–c has been limited to the periods from August to March 2017–2018 and 2018–2019, excluding time steps with zero snow depth (based on the model simulations) and time steps with wet snow (detected by S1, **excluding data when the wet snow fraction is larger than 0.5**). Consistent with the results shown in Figs. 2–4, the correlations for areas with a maximum snow depth above $\sim$1 m are considerably higher for γ^0_{VH} (Fig. 5b) than for γ^0_{VV} (Fig. 5a), often reaching values above 0.6. The time series correlation is generally higher for S1 snow depth (Fig. 5c) than for γ^0, with values often reaching above 0.8. This higher correlation results from the use of a ratio between γ^0 in cross- and co-polarization as input to the change detection algorithm and from the re-initialization (i.e., HS=0) at the start of every snow season, which removes differences in γ^0 levels between years. Fig. 5d further shows the correlation between the simulated and S1 snow depth with the inclusion of zero snow depths. This results in even higher correlations mainly in regions with shallow and occasional snow (e.g., in eastern Austria). Nevertheless, it is important to remark that the S1 γ^0 observations in these regions only show a weak (if any) correspondence with snow depth, because of the weak scattering contributions from shallow snow, frequent wet snow and melt conditions, and the frequent disappearance and re-appearance of snow cover. The higher correlation values are therefore

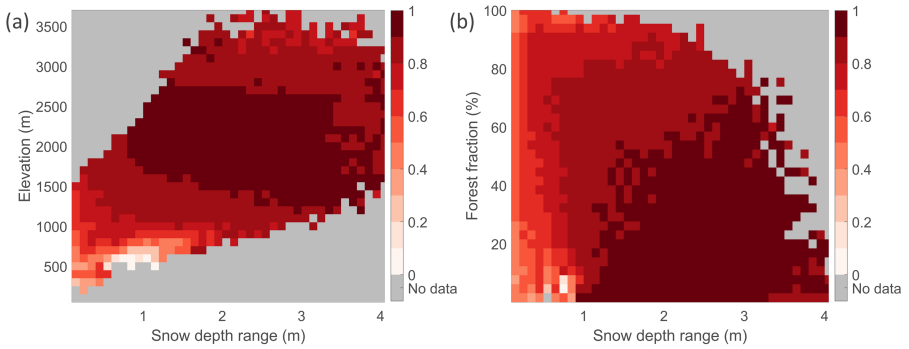

Figure 6. The time series correlation between weekly simulated and retrieved snow depth (m), stratified by (a) elevation (m) and snow depth range (m), and (b) forest cover fraction (%) and snow depth range (m).

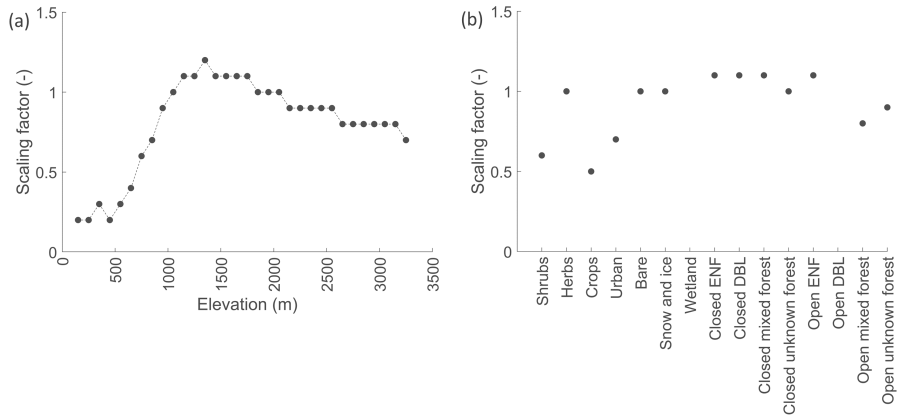

Figure 7. Scaling factor (E_2) for the conversion from SI (dB) into snow depth (m), stratified by (a) elevation and (b) land cover class. The scaling factors are derived after applying the constant scaling factor ($E_1 = 0.45\,\mathrm{m\,dB^{-1}}$; see Section 2.2).

mainly attributed to the effectiveness of the IMS snow cover data set, used as auxiliary input in the retrieval, to discern between the absence and presence of snow, and should thus not be attributed to the S1 observations.

Figure 6 stratifies the time series correlations of Fig. 5d by snow depth range (based on the model simulations), as well as elevation (from SRTM) and forest cover fraction (from the Copernicus PROBA-V dataset). The correlation generally exceeds **0.8** when the range in snow depth exceeds ∼1 m, except in areas with an elevation below ∼1000 m or a forest cover fraction above ∼80%. The S1 retrievals are thus expected to be more accurate for the high snow regime (with snow depths reaching above 1 m), and in areas with lower forest cover fraction.

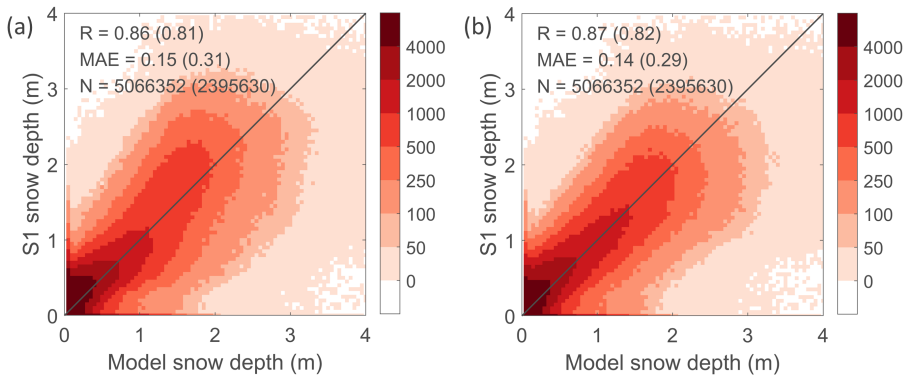

Figure 8. Density plots comparing weekly S1 retrievals of snow depth (m) with corresponding model simulations (m) for August through March 2017–2018 and 2018–2019 (data with a wet snow fraction larger than 0.5 excluded). Retrievals are derived using (a) spatially constant (E_1) and (b) spatially dynamic (E_2) scaling factors. The spatio-temporal Pearson correlation R (-), the MAE (m) and number of data (N) are shown on top left, both for scenarios with and (between brackets) without the inclusion of zero values.

3.1.3 Scaling to snow depth

The S1 snow depth retrievals depend on a scaling factor E, which is either constant (E_1), or spatially varying (E_2), and **is derived from the** model simulations. Figure 7 shows the scaling factor E_2 stratified per elevation band and per land cover class (see Section 2.2). The optimization of the scaling factor by elevation indicates a correction towards lower snow depth retrievals **primarily** at low elevations (below $\sim$1000 m), but also at high elevations (above $\sim$2500 m). At the low elevations, the signal-to-noise-ratio of the snow volume scattering is expected to be low due to the typically shallow snow conditions. Therefore, noise (or unaccounted impacts in the retrieval) can lead to an overestimation. **At the high elevations, the lower scaling factors likely correct for the relatively stronger decreases in γ^0_{VV} (see section 3.1.1) and therefore increases in γ^0_{CR}. The optimization of the scaling factor by land cover indicates that generally lower values are favorable in regions with shrubs and crops, and in urban areas, whereas slightly higher values are favorable in closed forests. The latter potentially compensates for the underestimation due to the attenuation of the snow signal by forests.**

Figure 8 compares the correspondence between S1 retrievals and model simulations of snow depth obtained with the constant scaling factor E_1 and with the spatially dynamic scaling factor E_2. It demonstrates the overall similarity in the snow depth estimates from the retrievals and simulations, and the slight improvement that results from the use of the spatially dynamic scaling factor. The spatially dynamic scaling factor is used for the retrievals in the next section and the validation with in situ measurements.

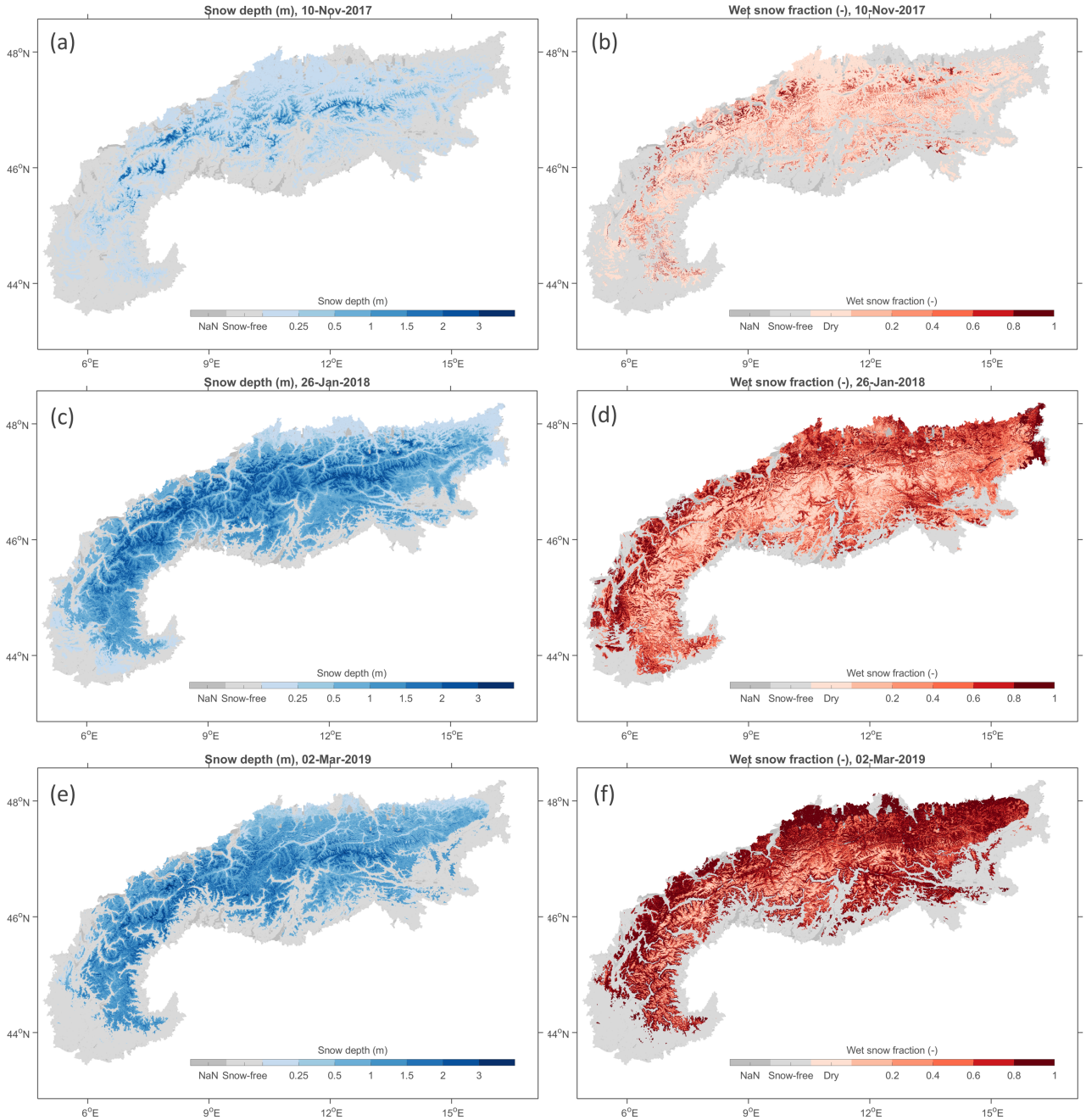

Figure 9. S1 snow depth (m) and **fractional wet snow cover (-)** retrievals at 300 m spatial resolution over the Alps, for the weeks centered around (a) 10/11/2017, (b) 26/01/2018 and (c) 02/03/2019.

3.2 Validation of sub-kilometer S1 retrieval with in situ measurements

Figure 9 shows examples of the S1 retrievals **of snow depth and wet snow fraction** over the Alps at the 300 m spatial resolution for the weeks centered around 10/11/2017, 26/01/2018 and 02/03/2019. The S1 retrievals for instance capture the strong increase in snow depth during winter 2017–2018 (Fig. 9a,c). The Alps experienced several episodes of extreme snowfall in January 2018, caused by a low-pressure system over the western Mediterranean that brought moist air northwards and resulted in an anomalously deep snowpack. The winter 2018–2019 was generally warmer than average, caused by a persistent high pressure system over western Europe. The warm temperatures led to extensive wet snow conditions during February, that were detected by S1 (Fig. 9f) **and can be used for masking the corresponding snow depth retrievals**. Unlike in the northern Alps, where the wet snow occurrence is widespread on 02/03/2019, wet snow is **more pronounced on** south facing slopes in the southern Alps.

The S1 snow depth retrievals at the three different spatial resolutions (100 m, 300 m and 1 km) **and with different levels of wet snow masking** are compared against independent point-scale in situ measurements over the periods August through March 2017–2018 and 2018–2019 (Fig. 10). Although the more detailed retrievals at the finer 100 m resolution have the potential to better represent the local point-scale conditions at the in situ sites, a higher accuracy is obtained at the coarser 300 m and 1 km resolutions. The lower accuracy for the finer-scale retrievals can be caused by the larger impacts of: (i) radar speckle that is inherent to radar measurements, (ii) geolocation errors and geometric distortions (foreshortening, layover) in the radar images causing location mismatches in γ^0 time series, and (iii) local heterogeneity in topography (elevation, slope, aspect), land surface properties (land cover, soil moisture, soil temperature and surface roughness) and snow variables (stratigraphy and microstructure). The 300 m retrievals offer a potential balance between resolution and accuracy. **The resolution is sufficiently high to capture the high spatial variability in snow depth at the hill-slope scale, while the accuracy (spatio-temporal R=0.86, MAE=0.17 m, for wet snow fraction below 0.5) is only slightly lower compared to the coarser 1 km scale (R=0.89, MAE=0.14 m).** However, the resolution requirement may depend on the envisaged application. For instance, the 1 km resolution may be too coarse for operational water management, but more than sufficient for regional numerical weather prediction. **A more stringent masking of wet snow conditions further improves the performance of the retrievals, increasing the spatio-temporal correlation and reducing the MAE, but also reduces the number of data.**

Figure 11 shows the temporal correlation and spatial correlation between the S1 retrievals and in situ measurements, stratified by the range in snow depth. In agreement with the comparison against model simulations (Section 3.1), the temporal correlation increases with the snow depth range, reaching consistently high values (0.8–0.95) for sites with snow depths reaching above 1 m. Similarly, the spatial correlation increases with increasing snow depth range, reaching values of ∼0.6–0.8 when measurements above ∼1.5 m are included.

Figure 12 shows the MAE and bias (measurements minus retrievals), both as absolute values and relative to the measured snow depth. The MAE of the 1 km retrievals increases slightly from ∼0.3 m at 0.5 m depth (60 %) to ∼0.5 m at 2.5 m depth (20 %), and then more abruptly to 1.3 m at 3.5 m depth (37 %). The absolute bias indicates a minor overestimation by S1 for low snow depths, which gradually reduces to no bias at 1.5–2 m depths. However, the corresponding

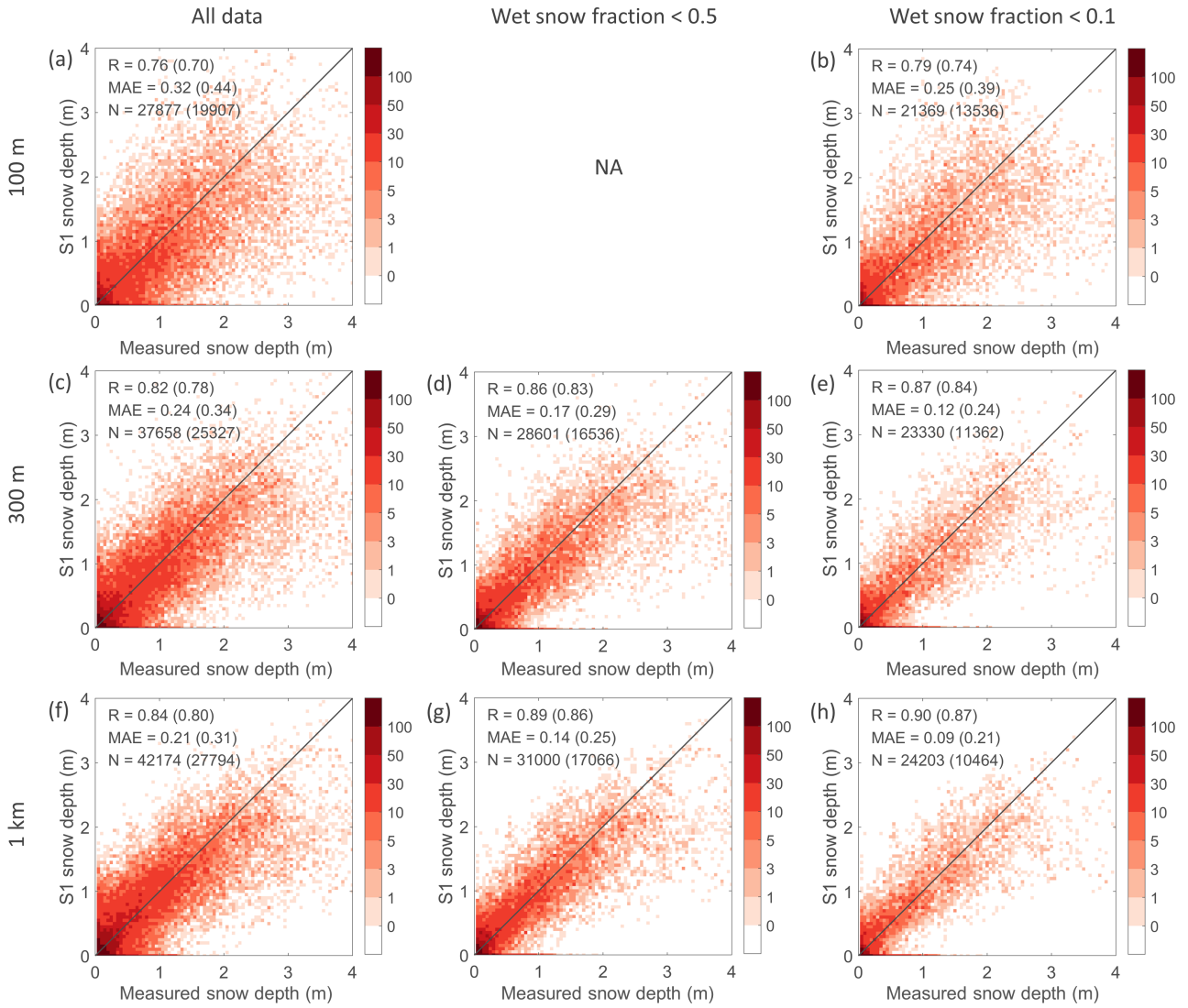

Figure 10. Density plots comparing weekly S1 retrievals of snow depth (m) with corresponding in situ measurements (m) for August through March 2017–2018 and 2018–2019. The comparison is shown for retrievals at (a,b) 100 m, (c,d,e) 300 m and (f,g,h) 1 km resolution, with (a,c,f) no wet snow masking applied, (d,g) the masking of data with a wet snow fraction larger than 0.5, and (b,e,h) the masking of data with a wet snow fraction larger than 0.1. The spatio-temporal Pearson correlation R (-), the MAE (m) and number of data (N) are shown on top left, both for scenarios with and (between brackets) without the inclusion of zero values. No result is shown for 100 m resolution and wet snow fraction < 0.5, as only binary (i.e., 0 or 1) wet snow information is available for the 100 m resolution.

relative biases for the low snow depths can be large due to the low measured values. An increasing underestimation occurs for higher snow depths, reaching $\sim$1.2 m bias at 3.5 m depth (35%). However, it is important to mention that

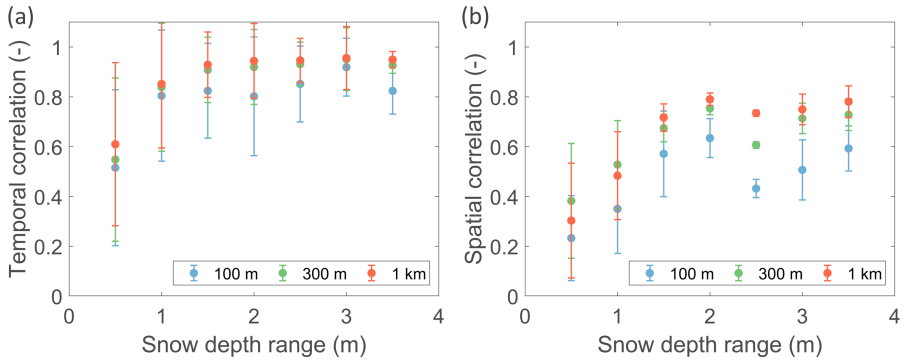

Figure 11. The (a) temporal and (b) spatial correlation between 100 m, 300 m and 1 km S1 retrievals and in situ measurements for August through March 2017–2018 and 2018–2019. Zero snow depth values and data with a wet snow fraction $\geq$ 0.5 are excluded. The metrics are stratified by the snow depth range (or maximum) of the measurements, and represent the mean value and standard deviation per 0.5 m interval. Note that for the temporal correlation, the mean and standard deviation are calculated from different locations in space, whereas for the spatial correlation, the metrics are calculated from different time steps.

part of the biases (and errors) can be due to the scaling of the retrievals based on model simulations and not based on in situ measurements (see Section 2.2). Indeed, the model simulations also show a very similar underestimation of the high snow depth measurements (data not shown). Furthermore, part of the biases and errors can be due to representativeness differences between the point-scale in situ measurements and the grid-scale satellite retrievals. For instance, in situ sites typically correspond with open flat field locations and often overestimate the mean snow depth of the surrounding terrain (Grünewald and Lehning, 2015). Intuitively, one would expect an improvement in skill for retrievals at a finer spatial scale (e.g., 100 m and 300 m). However, our results indicate the opposite. That is, the skill improves with coarser scales, although more when retrievals are aggregated from 100 m to 300 m, than from 300 m to 1 km. In general, this indicates that the potential improvement brought by the finer spatial scale of the retrieval can be offset by an increase in noise. In order to investigate the impacts of representativeness differences, future research is recommended to compare the S1 snow depth retrievals with validation data at the matching scale, such as snow depth estimates from LiDAR.

4 Conclusions

Sentinel-1 (S1) backscatter observations, particularly in VH-polarization, correlate well with regional model simulations of snow depth over Austria and Switzerland. Using a combination of cross-polarized and co-polarized backscatter as input to **an empirical** change detection algorithm, S1 snow depth retrievals at 100 m, 300 m and 1 km spatial and weekly temporal resolution are presented over the European Alps **for the periods from August through March 2017–2019**. The accuracy of the retrievals is validated using independent local time series measurements of snow depth at 743 locations across the Alps. Despite the typically large representativeness differences between these point-scale in situ measurements and grid-scale

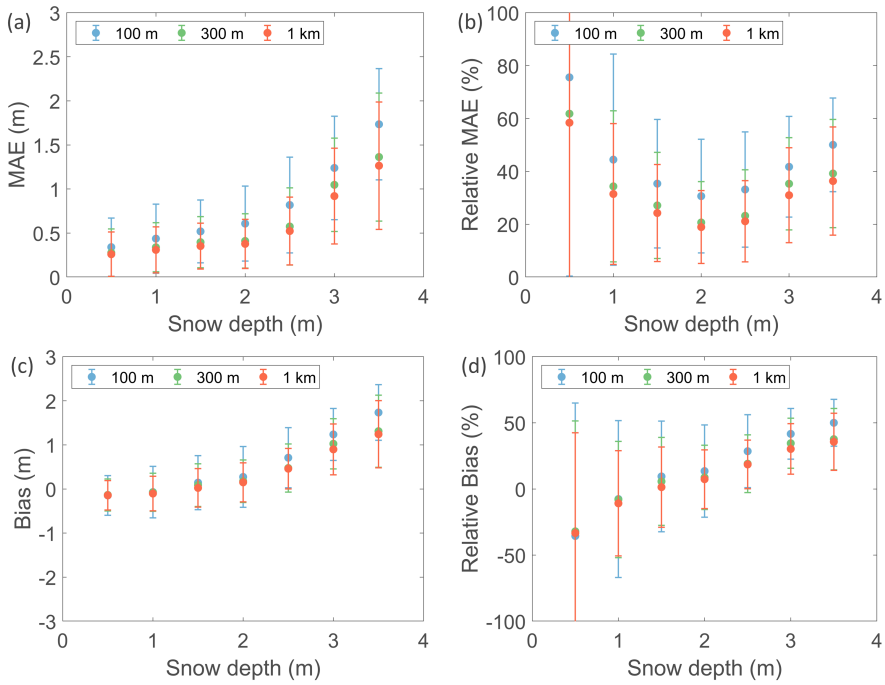

Figure 12. The (a) absolute MAE (m), (b) relative MAE (%), (c) absolute bias (m) and (d) relative bias (%) between 100 m, 300 m and 1 km S1 retrievals and in situ measurements for August through March 2017–2018 and 2018–2019. Bars indicate ± one standard deviation. Data with a wet snow fraction ≥ 0.5 are excluded. The metrics are stratified by the measured snow depth value (not by the range as in Fig. 11), with intervals of 0.5 m.

satellite retrievals, good skill metrics are obtained. **At the 1 km resolution and for primarily dry snow conditions (i.e., a wet snow fraction below 0.5), the spatio-temporal Pearson correlation coefficient equals 0.89 and the relative mean absolute error ranges between ∼20–30% for snow depths between 1 and 3 m. A slightly lower accuracy is observed at the 300 m and especially 100 m resolution.** The lower accuracy at the fine scale is likely caused by **increased impacts of measurement noise, geolocation errors and geometric distortions, and the local heterogeneity in topography, land surface and snow properties, such as microstructure and stratigraphy.**

The main uncertainties in the S1 snow depth retrievals are expected to be caused by wet, shallow and occasional snow cover and forest cover. Wet snow is known to cause a strong decrease in radar backscatter due to signal absorption. Although a wet snow detection algorithm is implemented, undetected wet snow (for instance due to an insufficient decrease in the backscatter) may cause underestimation in the snow depth retrievals. Uncertainties can also be large in regions with shallow and occasional snow cover, where the backscatter observations can be dominated by scattering contributions from the ground surface, resulting in a weak (or even negative) correlation with snow depth. For shallow snow conditions, backscatter observations at higher frequencies (e.g., X- or Ku-band), or potentially also using InSAR phase changes at lower (e.g., L- or P-band) frequencies,

could be more suitable to detect short-term snow depth changes. Higher uncertainties in the S1 retrievals may also be found in regions with large open water (lake) areal coverage, and in densely forested regions, where the attenuation of the radar signal may reduce the sensitivity to snow. The comparison of S1 retrievals with regional model simulations of snow depth reveals that sensitivity is generally strong (e.g., time series correlations >**0.8**) if the maximum snow depth reaches above ∼1 m, at an elevation above ∼1000 m or with a forest cover fraction below ∼80%.

The Sentinel-1 retrievals can provide important information on the spatial distribution of snow depth in regions with complex topography, which are typically excluded in passive microwave retrievals. Therefore, the results of this study may contribute to improving our knowledge on the terrestrial snow mass budget. An asset of the approach is the confirmed long-term availability of S1 observations, with continuity by S1C and S1D over the coming decades. This will allow for generating the long time series that are required for investigating the potential impacts of climate variability or climate change on snow mass in mountain regions and for assessing the corresponding impacts on water availability to society. Finally, the combination of the S1 retrievals with land surface model estimates through data assimilation is expected to be rewarding. Not only could the assimilation ensure improved and continuous (in time and space) estimates of mountain snow mass, it is also likely to benefit associated applications such as operational water management, natural hazard (avalanche and flood) prediction or numerical weather prediction.

Further research is needed to investigate more in depth the physical basis of C-band radar backscatter sensitivity to snow, for instance based on tower radar measurements and corresponding detailed measurements of snowpack properties, including snow microstructure and stratigraphy. Also, future research is recommended to investigate the validation of the S1 snow depth retrievals using data at the matching scale, for instance from LiDAR, and to further investigate the performance of the approach in other regions with different soil substrate types, vegetation conditions and snow climate conditions.

Data availability. The Sentinel-1 snow depth retrievals at 300 m and 1 km spatial and weekly temporal resolution are available online at https://ees.kuleuven.be/project/c-snow.

Author contributions. H. Lievens, I. Brangers, H.-P. Marshall and G. De Lannoy contributed to the Sentinel-1 snow depth retrieval algorithm. H. Lievens performed the analysis. T. Jonas and M. Olefs produced the snow model simulations and provided in situ measurements. All co-authors contributed to the writing of the manuscript.

Competing interests. No competing interests are present.

Acknowledgements. This work was funded through the BELSPO C-SNOW project. Sentinel-1A/B data are from the ESA and Copernicus Sentinel Satellites project and were processed using the ESA Sentinel Application Platform (SNAP). The resources and services used in this

work were provided by the VSC (Flemish Supercomputer Center), funded by the Research Foundation - Flanders (FWO) and the Flemish Government.

References

Arslan, A. N., Pulliainen, J., and Hallikainen, M.: Observations of L-and C-band backscatter and a semi-empirical backscattering model approach from a forest-snow-ground system, Progress In Electromagnetics Research, 56, 263–281, 2006.

Baghdadi, N., Gauthier, Y., and Bernier, M.: Capability of multitemporal ERS-1 SAR data for wet snow mapping, Remote Sensing of Environment, 60, 174–186, 1997.

Bernier, M. and Fortin, J.-P.: The potential of times series of C-band SAR data to monitor dry and shallow snow cover, IEEE Transactions on Geoscience and Remote Sensing, 36, 226–243, 1998.

Bernier, M., Fortin, J.-P., Gauthier, Y., Gauthier, R., Roy, R., and Vincent, P.: Determination of snow water equivalent using RADARSAT SAR data in eastern Canada, Hydrological Processes, 13, 3041–3051, 1999.

Blöschl, G.: Scaling issues in snow hydrology, Hydrological Processes, 13, 2149–2175, 1999.

Bormann, K. J., Brown, R. D., Derksen, C., and Painter, T. H.: Estimating snow-cover trends from space, Nature Climate Change, 8, 924–928, 2018.

Buchhorn, M., Smets, B., Bertels, L., De Roo, B., Lesiv, M., Tsendbazar, N.-E., Herold, M., and Fritz, S.: Copernicus Global Land Service: Land Cover 100m: collection 3: epoch 2018: Globe 2020, http://doi.org/10.5281/zenodo.3939050 [access date: 07/10/2020], 2020.

Chang, W., Tan, S., Lemmetyinen, J., Tsang, L., Xu, X., and Yueh, S. H.: Dense media radiative transfer applied to SnowScat and SnowSAR, IEEE Journal of Selected Topics in Applied Earth Observations and Remote Sensing, 7, 3811–3825, 2014.

Conde, V., Nico, G., Mateus, P., Catalão, J., Kontu, A., and Gritsevich, M.: On the estimation of temporal changes of snow water equivalent by spaceborne SAR interferometry: a new application for the Sentinel-1 mission, Journal of Hydrology and Hydromechanics, 67, 93–100, 2019.

de Rosnay, P., Balsamo, G., Albergel, C., Muñoz-Sabater, J., and Isaksen, L.: Initialisation of land surface variables for numerical weather prediction, Surveys in Geophysics, 35, 607–621, 2014.

Dechant, C. and Moradkhani, H.: Radiance data assimilation for operational snow and streamflow forecasting, Advances in Water Resources, 34, 351–364, 2011.

Dozier, J., Bair, E. H., and Davis, R. E.: Estimating the spatial distribution of snow water equivalent in the world's mountains, WIREs Water, 3, 461–474, 2016.

Du, J., Shi, J., and Rott, H.: Comparison between a multi-scattering and multi-layer snow scattering model and its parameterized snow backscattering model, Remote Sensing of Environment, 114, 1089–1098, 2010.

Essery, R., Morin, S., Lejeune, Y., and Ménard, C. B.: A comparison of 1701 snow models using observations from an alpine site, Advances in Water Resources, 55, 131–148, 2013.

Foster, J. L., Sun, C., Walker, J. P., Kelly, R., Chang, A., Dong, J., and Powell, H.: Quantifying the uncertainty in passive microwave snow water equivalent observations, Remote Sensing of Environment, 94, 187–203, 2005.

Frey, S. and Holzmann, H.: A conceptual, distributed snow redistribution model, Hydrology and Earth System Sciences, 19, 4517–4530, 2015.

Gelaro, R., McCarty, W., Suárez, M. J., Todling, R., Molod, A., and co-authors: The Modern-Era Retrospective Analysis for Research and Applications, Version 2 (MERRA-2), Journal of Climate, 30, 5419–5454, 2017.

Girotto, M., Musselman, K. N., and Essery, R. L. H.: Data assimilation improves estimates of climate-sensitive seasonal snow, Current Climate Change Reports, 6, 81–94, 2020.

Griessinger, N., Schirmer, M., Helbig, N., Winstral, A., Michel, A., and Jonas, T.: Implications of observation-enhanced energy-balance snowmelt simulations for runoff modeling of Alpine catchments, Advances in Water Resources, 133, 103 410, 2019.

Grünewald, T. and Lehning, M.: Are flat-field snow depth measurements representative? A comparison of selected index sites with areal snow depth measurements at the small catchment scale, Hydrological Processes, 29, 1717–1728, 2015.

Guneriussen, T., Høgda, K. A., Johnsen, H., and Lauknes, I.: InSAR for estimation of changes in snow water equivalent of dry snow, IEEE Transactions on Geoscience and Remote Sensing, 41, 230–242, 2001.

Haslinger, K. and Bartsch, A.: Creating long-term gridded fields of reference evapotranspiration in Alpine terrain based on a recalibrated Hargreaves method, Hydrology and Earth System Sciences, 20, 1211–1223, 2016.

Helbig, N., van Herwijnen, A., Magnusson, J., and Jonas, T.: Fractional snow-covered area parameterization over complex topography, Hydrology and Earth System Sciences, 19, 1339–1351, 2015.

Hiebl, J. and Frei, C.: Daily temperature grids for Austria since 1961 — concept, creation and applicability, Theoretical and Applied Climatology, 124, 161–178, 2016.

Hiebl, J. and Frei, C.: Daily precipitation grids for Austria since 1961 — development and evaluation of a spatial dataset for hydro-climatic monitoring and modelling, Theoretical and Applied Climatology, 132, 327–345, 2018.

Immerzeel, W. W., Lutz, A. F., Andrade, M., Bahl, A., Biemans, H., and co-authors: Importance and vulnerability of the world's water towers, Nature, 577, 364–369, 2020.

Kelly, R. E., Chang, A. T., Tsang, L., and Foster, J. L.: A prototype AMSR-E global snow area and snow depth algorithm, IEEE Transactions on Geoscience and Remote Sensing, 41, 230–242, 2003.

King, J., Kelly, R., Kasurak, A., Duguay, C., Gunn, G., Rutter, N., Watts, T., and Derksen, C.: Spatio-temporal influence of tundra snow properties on Ku-band (17.2 GHz) backscatter, Journal of Glaciology, 61, 267–279, 2015.

Leinss, S., Wiesmann, A., Lemmetyinen, J., and Hajnsek, I.: Snow water equivalent of dry snow measured by differential interferometry, IEEE Journal of Selected Topics in Applied Earth Observations and Remote Sensing, 8, 3773–3790, 2015.

Leinss, S., Löw, S., Proksch, M., Lemmetyinen, J., Wiesmann, A., and Hajnsek, I.: Anisotropy of seasonal snow measured by polarimetric phase differences in radar time series, The Cryosphere, 10, 1771–1797, 2016.

Lemmetyinen, J., Derksen, C., Rott, H., Macelloni, G., King, J., and co-authors: Retrieval of effective correlation length and snow water equivalent from radar and passive microwave measurements, Remote Sensing, 10, 170, 2018.

Lievens, H., Demuzere, M., Marshall, H. P., Reichle, R. H., Brucker, L., and co-authors: Snow depth variability in the Northern Hemisphere mountains observed from space, Nature Communications, 10, 4629, 2019.

Luojus, K. P., Pulliainen, J., Metsamaki, S., and Hallikainen, M.: Snow-covered area estimation using satellite radar wide-swath images, IEEE Transactions on Geoscience and Remote Sensing, 45, 978–989, 2007.

Magnusson, J., Gustafsson, D., Hüsler, F., and Jonas, T.: Assimilation of point SWE data into a distributed snow cover model comparing two contrasting methods, Water Resources Research, 50, 7816–7835, 2014.

Manickam, S. and Barros, A.: Parsing synthetic aperture radar measurements of snow in complex terrain: scaling behaviour and sensitivity to snow wetness and landcover, Remote Sensing, 12, 483, 2020.

Marin, C., Bertoldi, G., Premier, V., Callegari, M., Brida, C., Hürkamp, K., Tschiersch, J., Zebisch, M., and Notarnicola, C.: Use of Sentinel-1 radar observations to evaluate snowmelt dynamics in alpine regions, The Cryosphere, 14, 935–956, 2020.

Meromy, L., Molotch, N. P., Link, T. E., Fassnacht, S. R., and Rice, R.: Subgrid variability of snow water equivalent at operational snow stations in the western USA, Hydrological Processes, 27, 2383–2400, 2013.

Nagler, T. and Roth, H.: Retrieval of wet snow by means of multitemporal SAR data, IEEE Transactions on Geoscience and Remote Sensing, 38, 754–765, 2000.

Nagler, T., Roth, H., Ripper, E., Bippus, G., and Hetzenecker, M.: Advancements for snowmelt monitoring by means of Sentinel-1 SAR, Remote Sensing, 8, 348, 2016.

National Ice Center: IMS daily Northern Hemisphere snow and ice analysis at 1 km, 4 km, and 24 km resolutions, Boulder, CO: National Snow and Ice Data Center, Digital media [access date: 23/12/2020], 2008.

Niu, G.-Y., Yang, Z.-L., Mitchell, K. E., Chen, F., Ek, M. B., and co-authors: The community Noah land surface model with multiparameterization options (Noah-MP): 1. Model description and evaluation with local-scale measurements, Journal of Geophysical Research, 116, D12 109, 2011.

Olefs, M., Koch, R., Schöner, W., and Marke, T.: Changes in snow depth, snow cover duration, and potential snowmaking conditions in Austria, 1961–2020 — A model based approach, Atmosphere, 11, 1330, 2020.

Pellicciotti, F., Brock, B., Strasser, U., Burlando, P., Funk, M., and Corripio, J.: An enhanced temperature-index glacier melt model including the shortwave radiation balance: development and testing for Haut Glacier d'Arolla, Switzerland, Journal of Glaciology, 51, 573–587, 2005.

Pivot, F.: C-Band SAR imagery for snow-cover monitoring at treeline, Churchill, Manitoba, Canada, Remote Sensing, 4, 2133–2155, 2012.

Pulliainen, J., Luojus, K., Derksen, C., Mudryk, L., Lemmetyinen, J., and co-authors: Patterns and trends of Northern Hemisphere snow mass from 1980 to 2018, Nature, 581, 294–298, 2020.

RGI Consortium: Randolph Glacier Inventory - A Dataset of Global Glacier Outlines: Version 6.0., Global Land Ice Measurements from Space, Tech. rep., Colorado, USA, 2017.

Rott, H. and Nagler, T.: Capabilities of ERS-1 SAR for snow and glacier monitoring in alpine areas, in: Proceedings of the Second ERS-1 Symposium, pp. 1–6, Hamburg, Germany, 1993.

Rott, H., Yueh, S. H., Cline, D. W., Duguay, C., Essery, R., and co-authors: Cold regions hydrology high-resolution observatory for snow and cold land processes, Proceedings of the IEEE, 98, 752–765, 2010.

Schattan, P., Baroni, G., Oswald, S. E., Schöber, J., Fey, C., Kormann, C., Huttenlau, M., and Achleitner, S.: Continuous monitoring of snowpack dynamics in alpine terrain by aboveground neutron sensing, Water Resources Research, 53, 3615–3634, 2017.

Seidel, F. C., Rittger, K., Skiles, S. M., Molotch, N. P., and Painter, T. H.: Case study of spatial and temporal variability of snow cover, grain size, albedo and radiative forcing in the Sierra Nevada and Rocky Mountain snowpack derived from imaging spectroscopy, The Cryosphere, 10, 1229–1244, 2016.

Shi, J. and Dozier, J.: Estimation of snow water equivalence using SIR-C/X-SAR, part II: Inferring snow depth and particle size, IEEE Transactions on Geoscience and Remote Sensing, 38, 2475–2488, 2000.

Small, D.: Flattening gamma: radiometric terrain correction for SAR imagery, IEEE Transactions on Geoscience and Remote Sensing, 49, 3081–3093, 2011.

Small, D., Rohner, C., Miranda, N., Rüetschi, M., and Schaepman, M. E.: Wide-area analysis-ready radar backscatter composites, IEEE Transactions on Geoscience and Remote Sensing, in press, 2021.

Takala, M., Luojus, K., Pulliainen, J., Derksen, C., Lemmetyinen, J., Kärnä, J. P., Koskinen, J., and Bojkov, B.: Estimating Northern Hemisphere snow water equivalent for climate research through assimilation of spaceborne radiometer data and ground-based measurements, Remote Sensing of Environment, 115, 3517–3529, 2011.

Tedesco, M. and Narvekar, P. S.: Assessment of the NASA AMSR-E SWE Product, International Journal of Selected Topics in Applied Earth Observations and Remote Sensing, 3, 141–159, 2010.

Tsai, Y.-L. S., Dietz, A., Oppelt, N., and Kuenzer, C.: Wet and dry snow detection using Sentinel-1 SAR data for mountainous areas with a machine learning technique, Remote Sensing, 11, 895, 2019.

Ulaby, F. T., Moore, R. K., and Fung, A. K.: Microwave Remote Sensing: Active and Passive, Vol. II: Radar Remote Sensing and Surface Scattering and Emission Theory, Reading, MA: Addison-Wesley, 1982.

Vreugdenhil, M., Navacchi, C., Bauer-Marschallinger, B., Hahn, S., Steele-Dunne, S., Pfeil, I., Dorigo, W., and Wagner, W.: Sentinel-1 cross ratio and vegetation optical depth: A comparison over Europe, Remote Sensing, 12, 3404, 2020.

Winstral, A., Magnusson, J., Schirmer, M., and Jonas, T.: The bias-detecting ensemble: A new and efficient technique for dynamically incorporating observations into physics-based, multi-layer snow models, Water Resources Research, 55, 613–631, 2019.

Yueh, S. H., Dinardo, S. J., Akgiray, A., West, R., Cline, D. W., and Elder, K.: Airborne Ku-band polarimetric radar remote sensing of terrestrial snow cover, IEEE Transactions on Geoscience and Remote Sensing, 47, 3347–3364, 2009.

Zemp, M., Huss, M., Thibert, E., Eckert, N., McNabb, R., and co-authors: Global glacier mass changes and their contributions to sea-level rise from 1961 to 2016, Nature, 568, 382–386, 2019.